Wireless Condition Monitoring of Train Traction Systems Using Magnetoelectric Passive Current Sensors

Chung Ming Leung, Siu Wing Or, S. L. Ho, and K. Y. Lee

Abstract—**Novel power-supply-free, surface-mount-type magnetoelectric passive current sensors were developed and integrated with a 4-channel, 2.4-GHz wireless communication (transmitter and receiver) unit to form a new generation of wireless condition monitor for train traction systems. The wireless condition monitor was deployed in a field study on the East Rail Line in Hong Kong. Four pairs of magnetoelectric passive current sensors and single-channel wireless transmitters were installed, respectively, on and near the electric cables of four electric motor drives located underneath the 2nd, 5th, 8th, and 11th cars of a 12-car mainline train. The 4-channel wireless receiver was housed in the driver's cab of the train to provide real-time wireless monitoring of the current signatures of the four electric motor drives due to the operation of the train traction system in steady-state and acceleration conditions. The monitored current signatures were post-processed to obtain the distributions of the ratio of harmonic-to-fundamental current, their total harmonic distortions and power factors as well as the frequency spectra. A practical implication and correlation of the post-processed data with the operating conditions of the train traction system was established for application of the proposed wireless condition monitor as train traction system monitor.**

***Index Terms*—Electric motor drives, magnetoelectric passive current sensors, train traction systems, wireless communication unit, wireless condition monitoring.**

I. Introduction

Railway network is an iconic symbol of the growth and development of a society. The East Rail Line of MTR Corporation Limited (MTRCL), which was opened for passenger services in 1910, is the earliest urban public railway line in Hong Kong (Fig. 1) [1]. The Line was initially operated as a department of the Hong Kong Government until the establishment of Kowloon-Canton Railway Corporation (KCRC) in 1982. It served as the south section of the KCR network on the Hong Kong side, called the KCR British Section from 1910 to 1996, and the KCR East Rail from 1996 to 2007 after the act of construction of the KCR West Rail (now the West Rail Line) in the early 1990s. The north section to Canton (now Guangzhou) on the China side was known as the KCR Chinese Section (now the Guangzhou-Shenzhen Railway). The Line has been loaned to MTRCL and renamed from the KCR East Rail to the East Rail Line since the merger of KCRC into MTRCL under the Rail Merger Ordinance in 2007. Today, the Line has approximately 41 km of routes in service and consists of 14 stations starting at Hung Hom station in Kowloon and branching in the north at Sheung Shui station in the New Territories to terminate at either Lo Wu or Lok Ma Chau station for passenger and goods transport across the border between Hong Kong and Shenzhen, China [1],[2]. It carries an average of 800,000 passengers every day and allows a maximum service speed of 120 km/h.

Fig. 1. A 12-car mainline train operated by MTR Corporation Limited (MTRCL) on the East Rail Line in Hong Kong.

The electric catenary system adopted for the East Rail Line is a 25-kV, 50-Hz, single-phase ac overhead current collection system, which supplies up to 33 mainline trains per hour per direction [3],[4]. The electricity for the electric catenary system is taken from CLP Power Hong Kong Limited through 132/25-kV single-phase transformers with open-delta connection. Table I shows the specifications of a typical 12-car mainline train serving the East Rail Line as in Fig. 1 [4]. A mainline train consists of 12 cars with the total length of 285 m and the total capacity of 3,718 passengers. It has the maximum service speed of 120 km/h with acceleration and deceleration of 2.0 and 3.6 km/h/s, respectively. The train traction system has four sets of dc induction traction motors (GEC G315) and

This work was supported by the Research Grants Council of the HKSAR Government (PolyU 5228/13E) and The Hong Kong Polytechnic University (1-ZV7P).

C. M. Leung, S. W. Or, and S. L. Ho are with the Department of Electrical Engineering, The Hong Kong Polytechnic University, Hung Hom, Kowloon, Hong Kong (e-mail: eeswor@polyu.edu.hk).

K. Y. Lee is with MTR Corporation Limited, MTR Headquarters Building, Telford Plaza, Kowloon Bay, Kowloon, Hong Kong.

TABLE I
SPECIFICATIONS OF A TYPICAL 12-CAR MAINLINE TRAIN FOR SERVING THE EAST RAIL LINE AS IN FIG. 1 [4].

Parameter	Value
Number of Cars	12
Length	285 m
Width	3.1 m
Height	4.7 m
Number of doors per side per car	5
Total capacity of passengers	3,718
Maximum service speed	120 km/h
Acceleration	2.0 km/h/s
Deceleration	3.6 km/h/s
Train traction system	4 sets of dc induction traction motor (GEC G315) and thyristor-controlled electric motor drive
Power output per traction motor	225 kW
Total output power	900 kW
Electric catenary system	25-kV, 50-Hz, single-phase ac overhead current collection system

thyristor-controlled electric motor drives, which are installed underneath the 2nd, 5th, 8th, and 11th cars of the train and supplied electrically by the electric catenary system. Each traction motor carries an output power of 225 kW, making the total output power of 900 kW for a train.

Because of the high complexity, usage, and rating of the train traction systems, it is generally impracticable to avoid electrical and mechanical faults, and the effects may become more significant at high service speeds. The faults related to pantographs, motor drives, traction motors, gears, etc. have been discussed in recent years, and some preventive measures have been proposed [5]−[8]. Nonetheless, real-time monitoring of the operating conditions of train traction systems still remains a bottleneck that impedes an effective operation of modern railway networks in terms of safety, reliability, and availability [9]. It is especially important to provide an instant or even an early notification to railway/train operators about abnormality. Among various physical properties, current signatures governed by electric motor drives of train traction systems are regarded as the most informative and easily measured one for describing the actual operating conditions of the train traction systems [10]. In fact, current signature analysis has become an useful tool for fault detection of electric machines [11],[12].

From the perspective of condition monitors, traditional wired condition monitors are rather bulky in size and complicated in installation and maintenance as they not only require a proper placement of active sensors (e.g., Hall sensors) on desired locations, but also involve multiple connections between the active sensors and their power supplies, signal conditioners, and base station through power and signal cables. These problems, together with the large spatial size (e.g., long train length), tough and complex system connections (e.g. traction systems), critical measuring locations (i.e., underneath trains), hazardous operating environment (e.g., high-voltage and heavy-current environment), etc. of modern mainline trains, always create great challenges in the installation and implementation of the traditional wired condition monitors [9],[13]. By contrast, wireless condition monitors including the integration of active sensors with microcontrollers and wireless communication (transmitter and receiver) units, all powered by power packs or batteries, have emerged as a flexible alternative to the traditional wired condition monitors due to the ease of installation, large scalability, and highly distributed nature. However, the critical problem of using the wireless condition monitors in train traction systems is the powering of the active sensors in hazardous operating environments involving high voltages and heavy currents with strong electromagnetic fields [9],[13].

In view of the above, we have developed a novel class of current sensors, called magnetoelectric (ME) passive current sensors, which features power-supply-free, high-sensitivity, high-linearity, and wideband capabilities, based on the detection of vortex magnetic fields associated with current-carrying cables in accordance with Ampère's law as well as the giant ME effect in ME composite sensing elements [14]. In our previous work, we have announced our success in integrating four surface-mount-type ME passive current sensors with a 4-channel, 2.4-GHz wireless communication (transmitter and receiver) unit to form a new generation of wireless condition monitor for train traction systems as well as in capturing real time and wirelessly the current signatures associated with electric cables of the four electric motor drives located underneath the 2nd, 5th, 8th, and 11th cars of a 12-car mainline train running on the East Rail Line of MTRCL in Hong Kong [15]. In this paper, we not only disclose the technical details on the design, structure/configuration, operating principle, testing, and performance of the ME passive current sensors and the wireless communication unit, but also give a comprehensive analysis of the captured current signatures in terms of the distributions of the ratio of harmonic-to- fundamental current, total harmonic distortion, power factor, and frequency spectrum when the train traction system is in steady-state (with the traction motors de-energized) and acceleration (with the traction motors energized) conditions. The correlation between the analyzed results with the operating conditions of the train traction system is made.

II. Magnetoelectric Passive Current Sensors

A. Structure and Operating Principle

Figure 2 shows the schematic diagram and photograph of a typical surface-mount-type ME passive current sensor developed for the present study. The sensor has a length of 22 mm, a width of 10 mm, a thickness of 9 mm, and a mass of 18 g. The compact and lightweight design is aimed to improve the flexibility of placement and installation as well as to minimize the effect of mass loading on electric cables. The core of the sensor is a custom-made ME composite sensing element of dimensions 12 mm × 6 mm × 3 mm, which is encapsulated in a polyurethane foam to have isolation from external vibrations, magnetically biased by a NdFeB magnet at 0.2 kOe to maximize its detection sensitivity, and enclosed in a brass case to have shielding from external electric fields. The signal leads of the ME composite sensing element is connected to a RG179 coaxial cable of 6-m long and with Bayonet Neill-Concelman (BNC) termination. All components are secured in the brass case by filling of insulating epoxy and then fastening of set screws. This configuration not only provides a convenient way for using the sensor, but also enables a reliable detection of

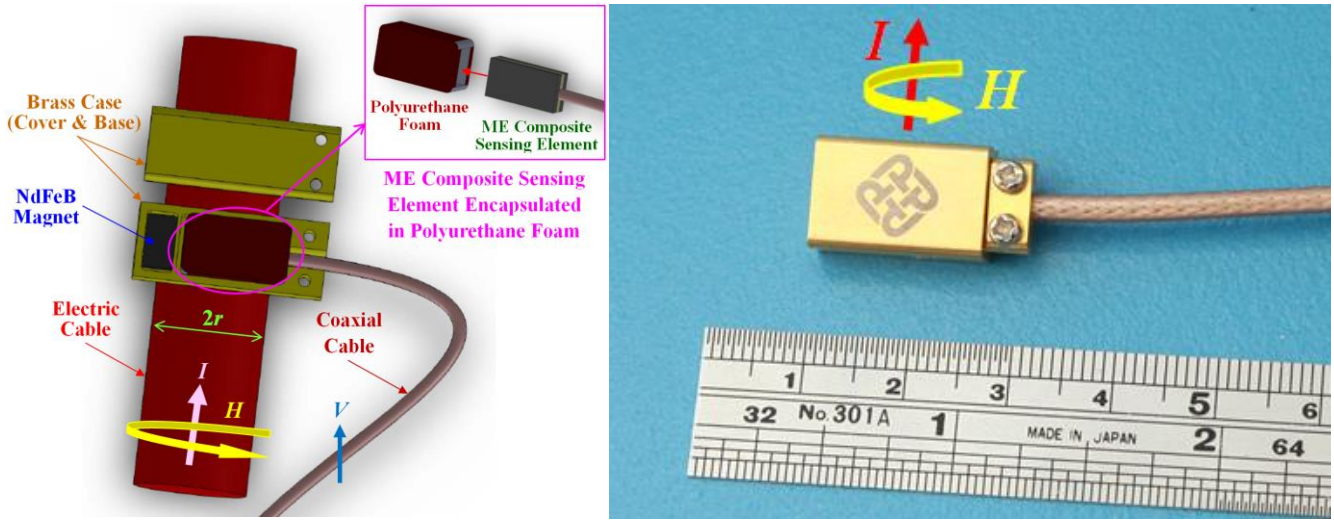

Fig. 2. Schematic diagram (left) and photograph (right) of a typical surface-mount-type magnetoelectric (ME) passive current sensor developed for the present study.

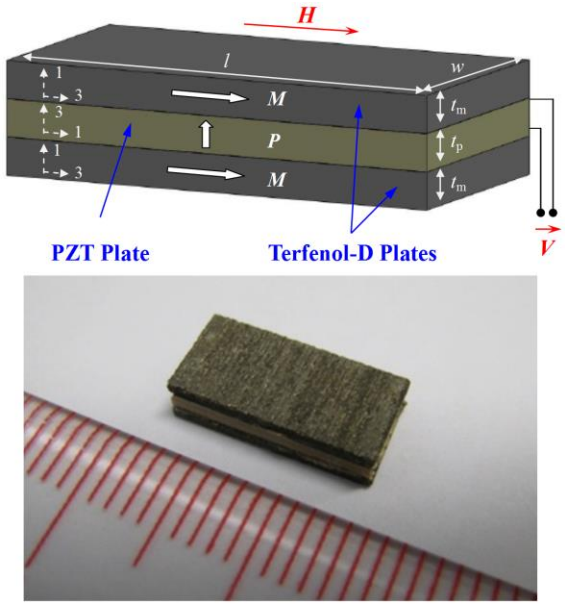

Fig. 3. Schematic diagram (upper) and photograph (lower) of ME composite sensing element used in the ME passive current sensor in Fig. 2. The arrows *M* and *P* denote the magnetization and polarization directions of the Terfenol-D and PZT plates, respectively.

magnetic fields governed by current-carrying electric cables through the shielding of electric field noise and the isolation of vibration noise.

The working principle of the sensor is as follows: when an ac electric current (*I*) is applied to an electric cable with a diameter (2*r*) in the axial direction as shown in Fig. 2, an ac vortex magnetic field (*H*) is induced along the length of the electric cable in accordance with Ampère's law as follows [16]:

$$H = \frac{I}{2\pi r}. \tag{1}$$

This *I*-induced *H*, which is detected by the ME composite sensing element of the sensor, is converted into an ac electric voltage (*V*) based on the giant ME effect in the ME composite sensing element characterized by the ME voltage coefficient (α_V) as follows [17]:

$$\alpha_V = \frac{dV}{dH}. \tag{2}$$

Combining Eqs. (1) and (2), the electric current sensitivity (S_I) of the sensor is

$$S_I = \frac{dV}{dI} = \frac{dV}{dH}\cdot\frac{dH}{dI} = \alpha_V \cdot \frac{1}{2\pi r}. \tag{3}$$

Figure 3 shows the structure and photograph of the ME composite sensing element used in the ME passive current sensor in Fig. 2. The sensing element is a sandwich-type composite material having a thickness-polarized Pb(Zr, Ti)O_3 (PZT) P8 piezoelectric ceramic plate of dimensions 12 mm (length: l) × 6 mm (width: w) × 1 mm (thickness: t_p) (supplied by CeramTec AG in Germany) sandwiched between two lengthwise-magnetized $Tb_{0.3}Dy_{0.7}Fe_{1.92}$ (Terfenol-D) magnetostrictive alloy plates of the same dimensions as the PZT plate (supplied by Baotou Rare Earth Research Institute, Inner Mongolia, China) along the thickness direction. The top and bottom Terfenol-D plates, when subjected to the *I*-induced *H* in Eq. (2), produces magnetostrictive strains along their length in the 3-direction based on the magnetostrictive effect. Because of the mechanical bonding between the Terfenol-D and PZT plates, these magnetostrictive strains, in turn, stress the central PZT plate, causing it to produce piezoelectric voltages (*V*) across its thickness in the 3-direction based on the piezoelectric effect. The product property of the magnetostrictive and piezoelectric effects, through mechanical mediation, gives rise to the modification of α_V in Eq. (2) and S_I in Eq. (3) to be [18]

$$\alpha_V = \frac{dV}{dH} = \frac{2d_{33,m}g_{31,p}t_m t_p}{s_{33}^H t_p + 2s_{11}^E t_m - 2d_{31,p}g_{31,p}t_m} \tag{4}$$

and

$$S_I = \frac{dV}{dI} = \frac{d_{33,m}g_{31,p}t_m t_p}{\pi r(s_{33}^H t_p + 2s_{11}^E t_m - 2d_{31,p}g_{31,p}t_m)}, \tag{5}$$

respectively, where t_m and t_p are the thicknesses of the Terfenol-D and PZT plates, respectively; $d_{33,m}$ and $d_{31,p}$ are the

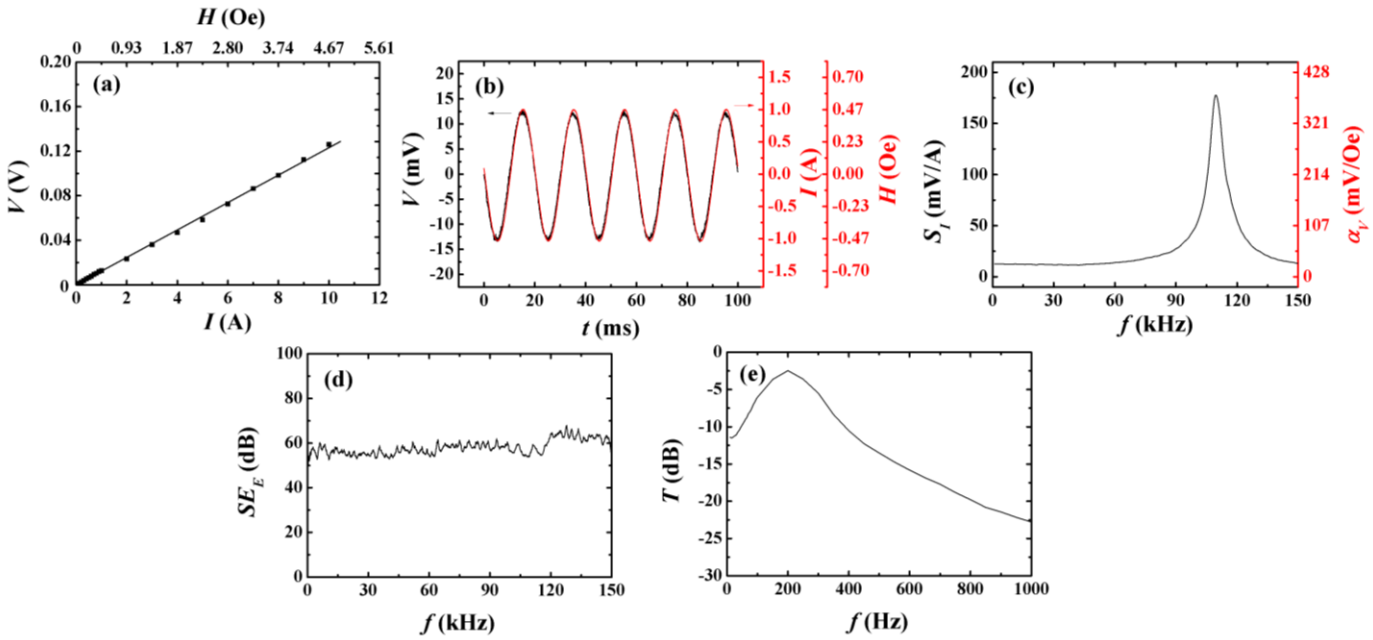

Fig. 4. Performance of ME passive current sensor in Fig. 2: (a) measured sensor voltage (V) as functions of applied cable current (I) and its associated vortex magnetic field strength (H) at a frequency of 50 Hz, (b) waveforms of V and I (and H) for I = 1 A at 50 Hz, (c) frequency (f) spectra of electric current sensitivity (S_I) and ME voltage coefficient (α_V), (d) f dependence of shielding effectiveness for electric fields (SE_E), and (e) f dependence of transmissibility of vibration (T).

piezomagnetic and piezoelectric strain coefficients, respectively; $g_{31,p}$ is the piezoelectric voltage coefficient; and s_{33}^H and s_{11}^E are the elastic compliance coefficients of the Terfenol-D and PZT plates, respectively. By substituting the material properties [19],[20] and geometric parameters of the Terfenol-D and PZT plates into Eqs. (4) and (5), α_V of the sensing element and S_I of the sensor are predicted to be 42 mV/Oe and 19 mV/A, respectively, at a frequency of 50 Hz with a magnetic bias of 0.2 kOe. The 50-Hz frequency corresponds to the fundamental driving frequency of the electric motor drives of the MTRCL's train traction systems to be discussed in section IV, while the 0.2-kOe magnetic bias represents the optimal magnetic bias field for the maximization of the magnetostrictive effect in the Terfenol-D plates, α_V of the sensing element, and hence S_I of the sensor [21].

B. Testing and Performance

The sensing performance of the developed ME passive current sensors (Fig. 2) was evaluated by mounting the sensors on an electric cable terminated with an 0.47-Ω resistor load to the ground and then energizing the electric cable with a sinusoidal current (I) in the amplitude and frequency ranges of 0.1–10 A peak and 25 Hz–150 kHz, respectively, using an arbitrary waveform generator (Agilent 33210A) connected to a supply amplifier (AE Techron 7796HF) operating in constant-current mode. A current probe (Hioki 9273) was clamped on the electric cable to measure I via a current amplifier (Hioki 3271). The voltage (V) output from the sensors was measured by a digital oscilloscope (LeCroy Waverunner 44Xi). The V–I characteristic, time-domain waveform, and electric current sensitivity (S_I) spectrum of the sensors were obtained and compared with the theoretical prediction in Eq. (5).

The electric field shielding performance of the sensors was examined by applying a sinusoidal voltage of 50 V peak over a prescribed frequency range of 25 Hz−150 kHz to an electric cable terminated with a 10-MΩ resistor load to ground using the arbitrary waveform generator connected to the supply amplifier operating in constant-voltage mode. The sensors to be measured were placed, in conjunction with an ME composite sensing element (Fig. 3), at a constant distance lateral to the length of the electric cable to experience a constant electric field strength of radiation of 114 V/m peak in the frequency range of 25 Hz−150 kHz. The voltage output from the sensors and the bare sensing element were measured by the digital oscilloscope. The frequency dependence of shielding effectiveness for electric fields (SE_E) of the sensors was determined by comparing the bare sensing element voltage with the sensor voltage in units of decibel [22].

The vibration isolation performance of the sensors was studied by mounting the sensors and the bare sensing element on a vibration exciter (B&K 4808) and then powering the vibration exciter to generate a sinusoidal vibration of constant acceleration of 10 m/s^2 along the thickness direction of the sensor and bare sensing element in the frequency range of 10–1000 Hz using a vibration exciter power amplifier (B&K 2719) controlled by a dynamic signal analyzer (SigLab 50-84). The acceleration was monitored using a laser vibrometer (Graphtec AT0042) connected to a laser signal demodulator (Graphtec AT3700). The voltage output from the sensors and the bare sensing element were measured by the dynamic signal analyzer. The frequency dependence of transmissibility of vibration (T) of the sensors was determined by comparing the sensor voltage with the bare sensing element voltage in units of decibel [23].

Figure 4(a) shows the measured sensor voltage (V) as functions of applied cable current (I) and its associated vortex magnetic field strength (H) at a frequency of 50 Hz. The values

of H were calculated based on Eq. (1). It is clear that V not only has a good linear response to I (and H), but also is very sensitive to the variation of I even at a small amplitude of 0.1 A. From the slope of the plot, the electric current sensitivity (S_I) of the sensors is determined to be 12.6 mV/A at 50 Hz, while the corresponding ME voltage coefficient (α_V) is found to be 27 mV/Oe. The measured S_I and α_V of the sensors are about one-third smaller than the calculated values of 19 mV/A and 42 mV/Oe using Eqs. (4) and (5), respectively, for the bare sensing elements (before being packaged as the sensors). Nonetheless, the output voltage and detection sensitivity of our sensors are 540–5400 times larger than those of the well-known Hall sensors of 5–50 μV/Oe [24]. Figure 4(b) plots the waveforms of V and I (and H) for I = 1 A at 50 Hz. It is seen that V is essentially clear and stable. It has an opposite phase with I (and H) because the piezoelectric coefficients $d_{31,p}$ and $g_{31,p}$ in Eqs. (4) and (5) both carry a negative sign. Nonetheless, the enhanced output signal strength and detection sensitivity, combined with the passive nature of our sensors, allow an autonomous and uninterrupted monitoring system to become feasible without the need of using power supplies and signal conditioners. Figure 4(c) gives the frequency spectrum of S_I (and α_V). Our sensors have an essentially flat response up to about 50 kHz. The significant enhancement in S_I (and α_V) at about 109 kHz is due to the occurrence of the fundamental shape (length) resonance in the sensing element of the sensors [17]. Nevertheless, our sensors have a wide operating frequency range up to 50 kHz. Figure 4(d) illustrates the frequency dependence of SE_E. The high SE_E in excess of 50 dB in the measured frequency range of 25 Hz–150 kHz indicates the presence of an effective shielding of external electric fields by the brass case in our sensors. This SE_E value is sufficiently large, and our sensors are sufficiently safe, to work in the train traction system environment. Figure 4(e) provides the frequency dependence of T. The generally negative value of T in the measured frequency range of 10–1000 Hz confirms the added vibration isolation effect in our sensors through the hysteresis damping in the polyurethane foam [25]. At 50 Hz where the electric motor drives of the MTRCL's train traction systems operate, T is as small as -10 dB, corresponding to an isolation of external vibrations in excess of 68%. For external vibrations higher than 400 Hz, our sensors have a more significant vibration isolation effect. Therefore, our sensors can effectively isolate the disturbance of trains' vibrations in the 10–1000 Hz of interest.

III. Wireless Communication Unit

Figure 5 shows the system block diagrams of the single-channel wireless transmitter and the 4-channel wireless receiver in the proposed 4-channel, 2.4-GHz wireless communication unit. A complete wireless communication unit consists of four single-channel wireless transmitters and one 4-channel wireless receiver, all powered by batteries. Each of the four single-channel wireless transmitters is composed of three functional modules, namely: signal conditioning module, central processing module, and wireless transmission module. The 4-channel wireless receiver contains four identical sets of

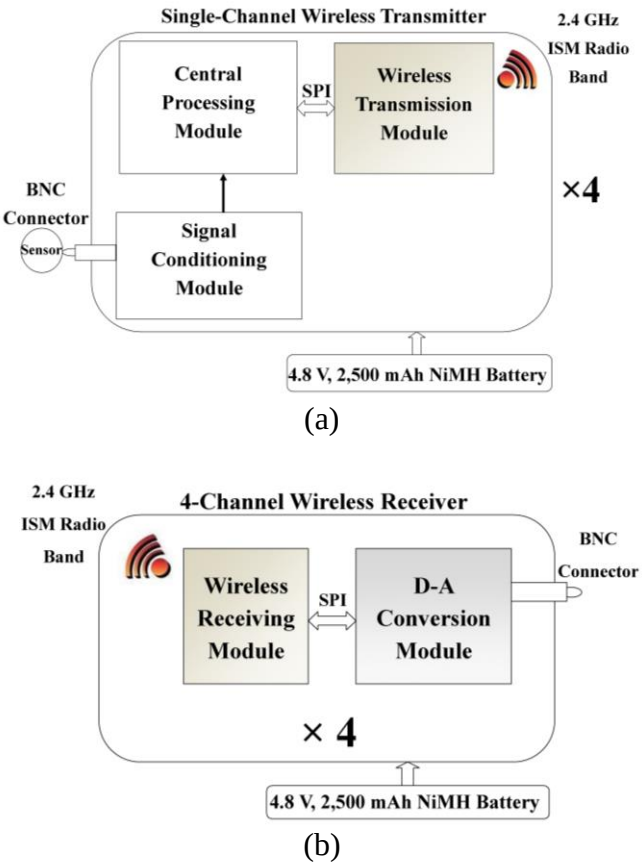

Fig. 5. System block diagrams of (a) single-channel wireless transmitter and (b) 4-channel wireless receiver (lower) in the proposed 4-channel, 2.4-GHz wireless communication unit

functional modules, namely: wireless receiving module and digital-to-analog (D-A) conversion module. In operation, each of the four 2.4 GHz communication channels (i.e., each of the four wireless transmitter and receiver pairs) functions at a unique frequency in the 2.4 GHz international industrial, scientific, and medical (ISM) radio band of 2.4000−2.4835 GHz [26]. On the side of the four single-channel wireless transmitters, the current signatures detected by the ME passive current sensors and in form of analog signals are coupled to the inputs of the wireless transmitters through BNC connectors before being transformed into a stable, determined, non-negative analog-signal format by the signal conditioning modules with amplification and dc-offsetting functions. The conditioned analog signals are converted into a usable digital-data format by the central processing modules, each comprising a microcontroller with the desired clock speed and an analog-to-digital (A-D) converter with the preferred A-D conversion resolution and sampling rate. The digital data is transferred to the wireless transmission module through the high-speed serial peripheral interface (SPI) port for wireless data transmission at the predetermined data transmission frequency (in the 2.4-GHz ISM radio band), rate, and power [26]. On the side of the 4-channel wireless receiver, the wireless data received by the wireless receiving module of each communication channel is converted into a usable analog-signal format by its D-A conversion module. The converted analog signals are coupled to the external means through BNC connectors. The operations of each

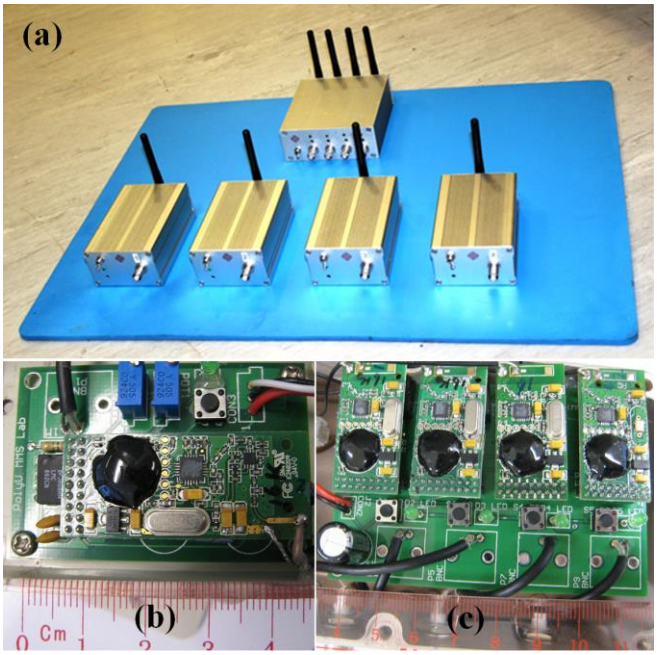

Fig. 6. Photographs of (a) the developed 4-channel, 2.4-GHz wireless communication unit, (b) the circuit board of one of the four single-channel wireless transmitters, and (c) the circuit board of the 4-channel wireless receiver.

single-channel wireless transmitter and each 4-channel wireless receiver are supported by 4.8-V, 2,500-mAh nickel-metal-hydride (NiMH) battery. The arrangement has a small operating power of less than 1.5 W, a long operating time in excess of 6 h, and a long communication range up to 300 m with a short delay time of less than 20 ms between the transmission and reception points.

Figure 6 displays the photographs of the developed wireless communication unit based on Fig. 5. The main components of the signal conditioning module, central processing module, and wireless transmission module in each of the four single-channel wireless transmitters are a National Semiconductor LMC662 CMOS operational amplifier, a Texas Instruments MSP430F2274 16-bit, ultralow-power microcontroller, and a Nordic Semiconductor nRF2401 single-chip radio transceiver with an ARGtek 1-W, 2.4-GHz booster radio-frequency (RF) amplifier, respectively. The LMC662 CMOS operational amplifier is configured as an inverting amplifier with a voltage gain of 10 and a dc offset of 2.5 V. The MSP430F2274 16-bit, ultralow-power microcontroller is a member of the MSP430 microcontroller family, featuring 16-bit data architecture, 16-MHz clock speed, and a build-in A-D converter of 10-bit conversion resolution and 200-k/s sampling rate. The 10-bit A-D conversion resolution is sufficient for most 50 Hz-based electrical-signal-sensing applications. The 200-k/s A-D sampling rate ensures that each sampling execution only takes 5 μs. The MSP430F2274 16-bit, ultralow-power microcontroller also provides a SPI port and a universal asynchronous receiver and transmitter (UART) port for interfacing with the wireless transmission module. The SPI port is used in our design. The nRF2401 single-chip radio transceiver is connected with an ARGtek 1-W, 2.4-GHz booster RF amplifier in the wireless transmission module. The nRF2401 single-chip radio

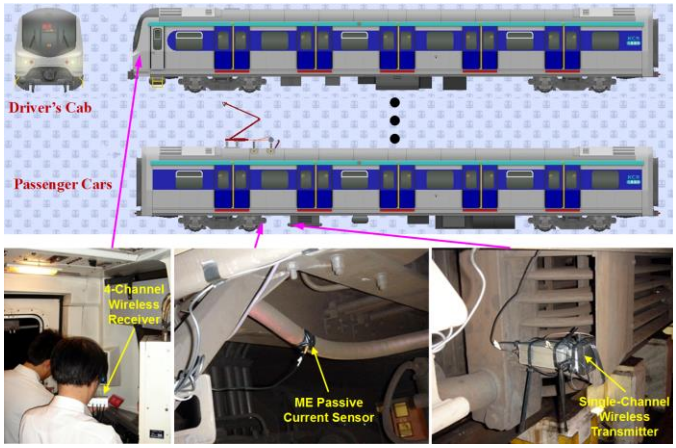

Fig. 7. Installation of the proposed wireless condition monitor in a 12-car mainline train operated by MTRCL on the East Rail Line in Hong Kong.

transceiver has a configurable data transmission rate up to 1 Mbps and is operated in the 2.4-GHz ISM radio band covering the 2.4000−2.4835 GHz frequency range. The ARGtek 1-W, 2.4-GHz booster RF amplifier is designed to amplify and transmit data at the nominal transmission frequency and power of 2.4 GHz and 1 W, respectively. For the 4-channel wireless receiver, the main components of the wireless receiving module and the D-A conversion module are a Nordic Semiconductor nRF2401 single-chip radio transceiver and an Analogy Device AD5542 16-bit D-A converter with a National Semiconductor LMC662 COMS operational amplifier. Upon receiving the wireless data (unsigned integer) from the nRF2401 single-chip radio transceiver in the wireless receiving module, the AD5542 16-bit D-A converter converts the integer values to non-negative analog signals before passing them to the LMC662 CMOS operational amplifier to generate bipolar analog signals in the D-A conversion module. The 1 μs D-A conversion settling time ensures that there is enough time for the stabilization of the D-A conversion process.

IV. Field Installation and Implementation

Four matched surface-mount-type ME passive current sensors (Fig. 2) were integrated with the 4-channel, 2.4-GHz wireless communication unit (Fig. 6) to form a new generation of wireless condition monitor for train traction systems. In our recent field study with MTRCL, the wireless condition monitor was deployed in the electric traction system of a 12-car mainline train operated by MTRCL on the East Rail Line in Hong Kong. As shown in Fig. 7, four pairs of ME passive current sensor and single-channel wireless transmitter were installed on/near the electric cables connecting the thyristor-controlled electric motor drives and the dc induction traction motors (GEC G315), all situated underneath the 2nd, 5th, 8th, and 11th cars, to detect and transmit the current signatures governed by the four electric motor drives of the electric traction system. A 4-channel wireless receiver was housed in the driver's cab of the train to receive the wirelessly transmitted current signatures. The received current signatures were displayed and recorded by an oscilloscope (LeCroy WaveRunner 44Xi) in the driver's cab. Post-processing of the current signatures acquired under operation of the train in

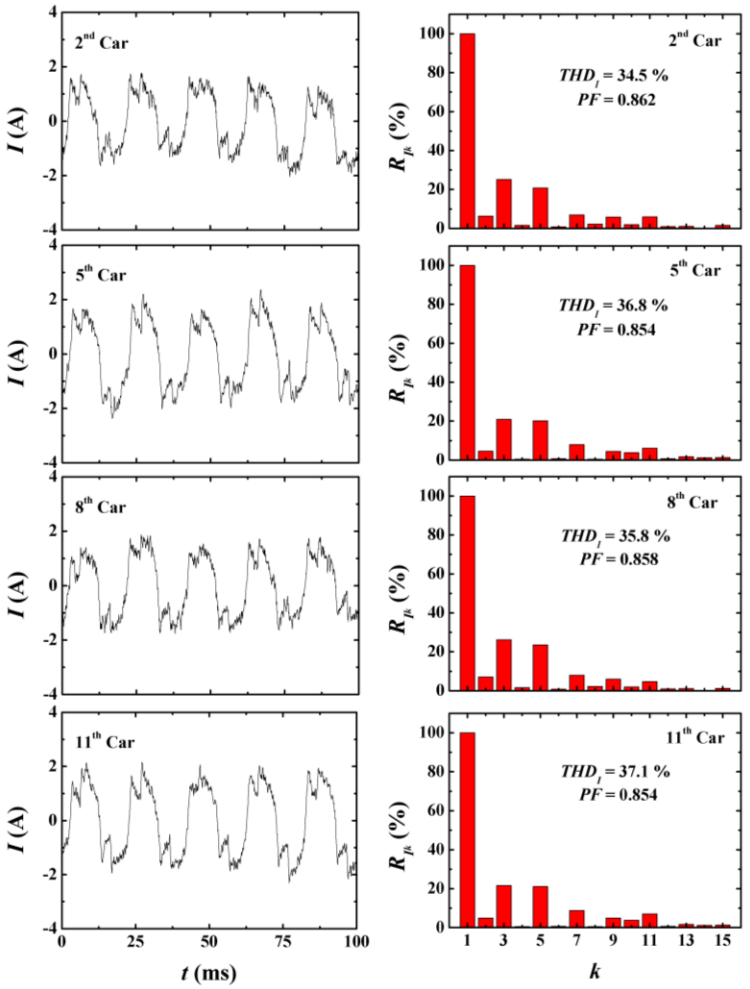

Fig. 8. Current signatures acquired by the proposed wireless condition monitor (left) and distributions of the ratio of harmonic-to-fundamental current (R_{I_k}) calculated using Eq. (6) (right) when the train traction system is in steady-state condition. The total harmonic distortion of the current signatures (THD_I) and power factor (PF) calculated using Eqs. (7) and (8), respectively, are also shown.

steady-state (with the traction motors de-energized) and acceleration (with the traction motors energized) conditions was implemented because of the greatest value for engineering services as well as systems and operation safety. The ratio of harmonic current (I_k) to fundamental current (I_1) was evaluated in accordance with [27]

$$R_{I_k} = \frac{I_k}{I_1}, \quad (6)$$

where $k \neq 1$ is the order of harmonic currents. The total harmonic distortion of the current signatures (THD_I), a figure-of-merit for quantifying the level of harmonics in current signatures, was calculated as the square root of the sum of the squares of the root-mean-square (rms) values of the harmonic currents (I_k) divided by the rms value of the fundamental current (I_1) [27]:

$$THD_I = \frac{\sqrt{\sum_{k=2}^{15} I_k^2}}{I_1}. \quad (7)$$

The power factor (PF) was deduced using the calculated THD_I as follows [25]:

$$PF = \frac{1}{\sqrt{1+THD_I}}. \quad (8)$$

V. Results and Analysis

Figure 8 shows the current signatures acquired by the proposed wireless condition monitor (Figs. 2 and 6), together with the distributions of R_{I_k} calculated using Eq. (6), when the train traction system is in steady-state condition. Figure 9 displays the results when the train traction system is in acceleration condition. It is clear that the current signatures captured in steady-state condition are physically different from those acquired in acceleration condition. When the train traction system is in steady-state condition, the current signatures have relatively small peak amplitudes of about 2 A for all cars because of the limited energy consumption in air conditioning, lighting, etc. (Fig. 8). The current signatures become more clearly and the peak amplitudes increase significantly to about 10 A when the train traction system is in acceleration condition (Fig. 9). The calculated R_{I_k} distributions for harmonic currents up to the 15th order vary from 0.2 to 27% in steady-state condition, but exhibit a higher magnitude with a larger variation of 0.3–67% in acceleration condition. The THD_I and PF values, as calculated using Eqs. (7) and (8), respectively, are found to have better values with smaller variations of 34–38% and 0.85–0.86 in steady-state condition compared to 51–66% and 0.77–0.81 in acceleration condition. The observation suggests the presence of larger loads or losses

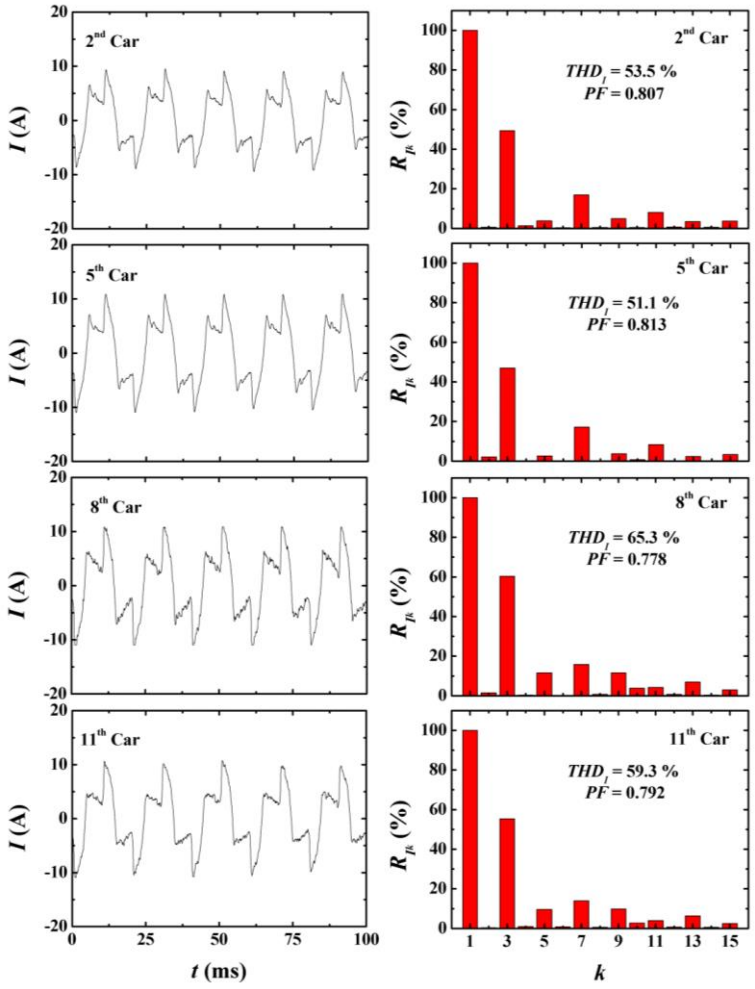

Fig. 9. Current signatures acquired by the proposed wireless condition monitor (left) and distributions of the ratio of harmonic-to-fundamental current (R_{I_k}) calculated using Eq. (6) (right) when the train traction system is in acceleration condition. The total harmonic distortion of the current signatures (THD_I) and power factor (PF) calculated using Eqs. (7) and (8), respectively, are also shown.

when the train traction system is in acceleration condition in comparison with the steady-state condition [28]. In both conditions, our wireless condition monitor is capable of acquiring reliable current signatures of all of the four electric motor drives in real time. Importantly, railway/train operators could determine immediately whether the train traction systems are running normally or not, especially whether all of the four electric motor drives and traction motors could be energized simultaneously in response to an acceleration command every time. If one or more electric motor drives or traction motors could not be energized simultaneously, the malfunctioned one(s) would increase the loading effect on the train which, in turn, would deteriorate the current signatures, R_{I_k} distributions as well as THD_I and PF values. With the aid of the wireless condition monitor, railway/train operators would be noticed in early about the abnormality, thereby minimizing the chance of in-service failure or even accident.

It is interesting to note that the current signatures of Fig. 8 contain a low-frequency signal which is amplitude-modulated with the 50-Hz electric motor driving currents as the envelopes. This low-frequency signal is not obvious in Fig. 9 when the train traction system is in acceleration condition. In order to have a physical insight into the low-frequency signal, the current signatures in both Figs. 8 and 9 are transformed into frequency spectra in Fig. 10. It is seen from Fig. 10(a) that the low-frequency signal has a frequency of about 15 Hz and an amplitude of about 0.15 A peak. This may be caused by the direct-coupling of the background vibration noise of the train to the piezoelectric layer of our ME passive current sensors. As shown in Fig. 4(e), our sensors can effectively isolate most of the vibration disturbance in the frequency range of 10–1000 Hz. The appearance of this 15-Hz, 0.15-A signal in the steady-state operation of the train represents a residual vibration noise, which is weak (1.5% only) in comparison with the electric motor driving currents of about 10 A peak in acceleration condition [Fig. 10(b)], and could be removed easily by adding a high-pass filter after the sensors.

VI. Conclusions and Future Work

We have developed a novel wireless condition monitor consisting of four power-supply-free, surface-mount-type ME passive current sensors and one 4-channel, 2.4-GHz wireless communication unit to provide real-time wireless monitoring of the current signatures of the four electric motor drives located underneath the 2nd, 5th, 8th, and 11th cars of a 12-car mainline train operated by MTRCL on the East Rail Line in Hong Kong. Four pairs of ME passive current sensors and single-channel wireless transmitters have been installed, respectively on and near electric cables associated with the four electric motor drives, while a 4-channel wireless receiver has been housed in the driver's cab. The current signatures due to the operation of the train traction system in steady-state and acceleration

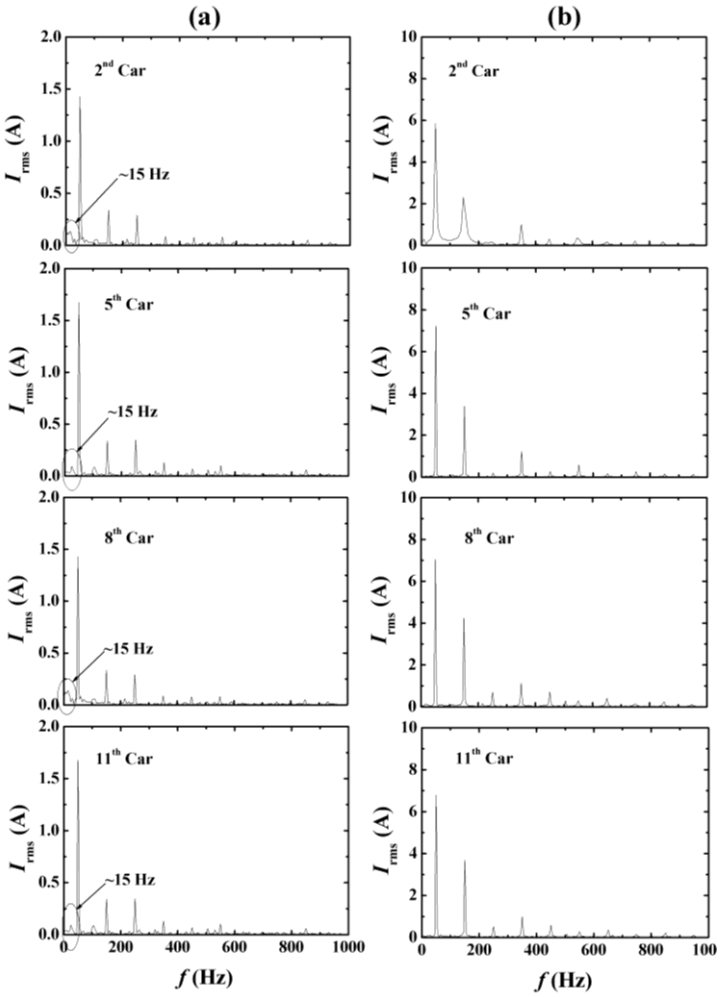

Fig. 10. Frequency spectra of the current signatures in (a) Fig. 8 and (b) Fig. 9.

conditions have been acquired by the wireless condition monitor. The distributions of R_{I_k} and their THD_I and PF have been calculated and analyzed. It has been found that all parameters obtained in steady-state condition have better values with smaller variations than those acquired in acceleration condition as a result of the increased loads or losses in acceleration condition. Our sensors have also demonstrated an effective shielding of electric field noise and an effective isolation of vibration noise, which make them suitable for real-time monitoring of train traction systems. Therefore, railway/train operators could determine in real time whether the train traction systems are running normally or not, especially whether all of the four electric motor drives and traction motors can be energized simultaneously by every acceleration command, by simply observing the wirelessly received current signatures as well as the post-processed R_{I_k}, THD_I, and PF values. Our proposed wireless condition monitor could provide railway/train operators an early notification about the abnormality, thereby minimizing the chance of in-service failure or even accident Work on further analysis of the current signatures to extract a more comprehensive understanding of system information is in progress.

REFERENCES

[1] Kowloon-Canton Railway Corporation. http://www.kcrc.com.

[2] T. K. Ho, "Railway engineering research in Hong Kong", *Proceedings International Symposium on Transportation Science and Engineering for Global Chinese Scholars*, Beijing, China, August 2003.

[3] Z. M. Ye, E. W. C. Lo, K. H. Yuen, P. Tang, and S. G. Ye, "A study of current harmonics of electrical traction power supply system", *Proceedings 31st IEEE Annual Power Electronics Specialists Conference*, vol. 3, pp. 1149–1152, June 2000.

[4] MTR Metro Cammell EMU(AC). http://en.wikipedia.org/wiki/East_Rail_Line_Metro_Cammell_EMU.

[5] S. Midya, D. Bormann, T. Schutte, and R. Thottappillil, "Pantograph arcing in electrified railways—Mechanism and influence of various parameters—Part II: With AC traction power supply", *IEEE Transactions on Power Delivery*, vol. 24, no. 4, pp. 1940–1950, 2009.

[6] J. Guzinski, H. Abu-Rub, M. Diguet, Z. Krzeminski, and A. Lewicki, "Speed and load torque observer application in high-speed train electric drive" *IEEE Transactions on Industrial Electronics*, vol. 57, no. 2, pp. 565–574, 2010.

[7] J. Cao, H. Cui, and N. Li, "Research on fault detection method and device of EMU traction motors", *Proceedings 2013 International Conference on Electrical and Information Technologies for Rail Transportation*, vol. 1, pp. 293–301, January 2014.

[8] H. Henao, S. H. Kia, and G. A. Capolino, "Torsional-vibration assessment and gear-fault diagnosis in railway traction system" *IEEE Transactions on Industrial Electronics*, vol. 58, no. 5, pp. 1707–1717, 2011.

[9] D. Barke and W. K. Chiu, "Structural health monitoring in the railway industry: a review", *Structural Health Monitoring*, vol. 4, no. 1, pp. 81–93, 2005.

[10] W. T. Thomson and M. Fenger, "Case histories of current signature to detect faults in induction motor drives", *Proceedings IEEE International Electric Machines and Drives Conference*, vol. 3, p. 1459–1465, June 2003.
[11] J. Royo, F. J. Arcega, "Machine current signature analysis as a way for fault detection in squirrel cage wind generators", *Proceedings IEEE International Symposium on Diagnostics for Electric Machines, Power Electronics and Drives*, pp. 269–272, September 2007.
[12] C. Bruzzese, "Validation of sequence circuits useful for split-phase current signature analysis (SPCSA) and diagnosis of eccentric-rotor traction cage motors", *Proceedings 3rd International Conference on Electric Power and Energy Conversion Systems*, pp. 1–8, October 2013.
[13] J. E. Amadi-Echensu, K. Brown, R. Willett, and J. Mathew, *Definitions, Concepts and Scope of Engineering Asset Management*, London: Springer, 2011.
[14] C. M. Leung, *Magnetoelectric Smart Current Sensors for Wireless Condition Monitoring Applications*, Ph.D. Thesis, The Hong Kong Polytechnic University, 2012.
[15] C. M. Leung, S. Y. Zhang, S. W. Or, S. L. Ho, and K. Y. Lee, "Magnetoelectric smart current sensors for wireless condition monitoring of train traction systems", Proceedings 1st International Workshop on High-speed and Intercity Railways, vol. 2, pp. 319–327, July 2011.
[16] R. F. Harrington, *Introduction to Electromagnetic Engineering*, NY: Dover, 2003.
[17] Y. Wang, J. Li, D. Viehland, "Magnetoelectrics for magnetic sensor applications: status, challenges and perspectives", *Materials Today*., 2014
[18] M. I. Bichurin, and V. M. Petrov, and G. Srinivasan, "Modeling of magnetoelectric interaction in magnetostrictive-piezoelectric composites", *Advances in Condensed Matter Physics*, 2012
[19] Baotou Rare Earth Research Institute data sheet. http://www.brire.com/brire/cpxx/cpxx.htm.
[20] CeramTec AG. http://www.ceramtec.com.
[21] W. He, P. Li, Y. Wen, J. Zhang, A. Yang, and C. Lu, "Note: A high-sensitivity current sensor based on piezoelectric ceramic Pb (Zr, Ti) O3 and ferromagnetic materials", *Review of Scientific Instruments*, *85*(2), 026110, 2014
[22] H. W. Ott, *Electricmagnetic Compatibility Engineering*, A John Wiley and Sons, New York, 2009.
[23] S. Goldman, *Vibration spectrum analysis: a practical approach*. Industrial Press Inc., 1999.
[24] E. Ramsden, *Hall-Effect Sensors: Theory and Applications*, 2nd Edition, Burlington, Oxford: Elsevier, 2006.
[25] S. W. White, S. L. Kim, A. K. Bajaj, P. Davies, D. K. Showers, and P. E. Liedtke, "Experimental techniques and identification of nonlinear and viscoelastic properties of flexible polyurethane foam", *Nonlinear Dynamics*, *22*(3), 281-313, 2000.
[26] D. D. Coleman and D. A. Westcott, *CWNA Certified Wireless Network Administrator Official Study Guide: Exam PW0-104*. John Wiley & Sons, 2009.
[27] L. Cividino, Power factor, harmonic distortion; causes, effects and considerations. In *Telecommunications Energy Conference, 1992. INTELEC'92., 14th International* (pp. 506-513), 1999.
[28] Z. M. Ye, E. W. C. Lo, K. H. Yuen, P. Tang, S. G. Ye, "A Study of Current Harmonics of Electrical Traction Power Supply System", *31st IEEE Annual Power Electronics Specialists Conference*, Vol. 3, pp. 1149–1152, 2000.

Chung Ming Leung received his B.Eng. and Ph.D. degrees in electrical engineering from The Hong Kong Polytechnic University in 2007 and 2012, respectively. He worked as an E-T-A-supported Postdoctoral Fellow from 2012 to 2014, and become a Scientific Officer in February 2014, both in the Department of Electrical Engineering at the University. His research interests include magneto-electro-mechanically coupled smart materials, sensors and actuators, energy harvesting, condition monitoring, and power electronics. He has published 30 SCI journal papers and 3 international conference papers. Dr Leung is a member of the Institution of Engineering and Technology, U.K.

Siu Wing Or received his B.Sc. (1st Class Honors), MPhil, and Ph.D. degrees in engineering physics from The Hong Kong Polytechnic University (PolyU) in 1995, 1997, and 2001, respectively. He was a Teaching Company Associate, an R&D Electronic Engineer, and a Senior R&D Electronic Engineer in ASM Assembly Automation Ltd., Hong Kong, from 1995 to 2001. He then worked as a Postdoctoral Research Fellow in the Mechanical and Aerospace Engineering Department at the University of California, Los Angeles, USA, for 1.5 years before he joined PolyU as a Lecturer in 2002. He is currently a Professor and the Director of Smart Materials and Systems Laboratory in the Department of Electrical Engineering at PolyU. His research interests include smart materials and devices in the bulk, micro-, and nano-scale, condition and structural health monitoring, energy harvesting and storage, electromagnetics, ultrasonics, and vibration control. He has about 250 publications, including several professional book chapters, 160 SCI journal papers, 50 international conference papers in addition to the award of 41 patents. Prof. Or is a senior member of IEEE.

S. L. Ho obtained his B.Sc. and Ph.D. degrees in electrical engineering from the University of Warwick, U.K., in 1976 and 1979, respectively. He has been with the Department of Electrical Engineering, The Hong Kong Polytechnic University since 1979, and is currently the Chair Professor in Electricity Utilization at the University. His research interests include condition monitoring of railway systems, novel sensors, optimization of electromagnetic devices, phantom loading of electrical machines as well as design and development of novel machines. He has published about 300 papers in SCI journals, mostly in IEEE Transactions and IET Proceedings, 250 international conference papers, and is the holder of several patents. Prof. Ho is a member of the Hong Kong Institution of Engineers.

K. Y. Lee obtained his AP(HK), M.Phil., and Eng.D. degrees from The Hong Kong Polytechnic University. He is currently the Chief of Operations Engineering in MTR Corporation Limited, Hong Kong, responsible for directing all engineering services in enhancing asset worth to business as well as ensuring asset management and renewal to meet safety, business, and customer requirements. He has over 29 years of experience in railway systems maintenance, design, and engineering practices. He is active in railway system research, particularly in condition-based monitoring of equipment, life-cycle asset management, systems and operation

assurance, and smart railway development. He holds several patents on fiber-optic sensors for railway monitoring. Dr Lee is a member of the Hong Kong Institution of Engineers and the Institute of Engineering and Technology, U.K.